



Narrowband, tunable, 2 μm optical parametric master-oscillator power amplifier with large-aperture periodically poled Rb:KTP

R. S. Coetzee¹ · X. Zheng² · L. Fregnani³ · F. Laurell¹ · V. Pasiskevicius¹

Received: 12 February 2018 / Accepted: 23 May 2018 / Published online: 31 May 2018
© The Author(s) 2018

Abstract

A high-energy, ns, narrow-linewidth optical parametric oscillator and amplifier system based on large-aperture periodically poled Rb:KTP is presented. The 2 μm seed source is a singly resonant OPO locked with a transversely chirped volume Bragg grating, allowing a wavelength tuning of ~ 21 nm and output linewidth of 0.56 nm. A maximum output energy of 52 mJ and conversion efficiency of 36% was obtained from the amplifier for a pump energy of 140 mJ. The high-energy and the robust and narrow dual-wavelength spectra obtained make this system an ideal pump source for difference frequency generation-based THz generation schemes.

1 Introduction

Development of high-energy, narrowband coherent mid-infrared sources has rapidly increased over the past few decades. This is largely motivated by the applications where these sources may serve, such as in LIDAR, surgery/medical and defense [1, 2]. These applications require tunable high-energy sources, while still maintaining excellent spectral and temporal characteristics. Typical sources which fulfill these criteria include 2 μm Tm³⁺/Ho³⁺-doped solid-state and fiber lasers, as well as parametric devices such as optical parametric oscillators (OPO) [3, 4]. OPOs are of considerable interest due to the ability to deliver high energies over a very broad tuning range, which is impossible or limited with other coherent sources. This radiation can be further amplified in optical parametric amplifier (OPA) stages, yielding the high energies required. Such a master-oscillator power

amplifier (MOPA) scheme allows for efficient energy extraction from the pump without sacrificing spectral and spatial quality of the generated radiation [5].

Many applications in spectroscopy and imaging, in security and biomedical fields, require quasi-CW and/or nano-second tunable coherent sources at even longer wavelengths of the electromagnetic spectrum, at frequencies between 0.5 and 10 THz [6–8]. There are a number of light sources available to reach into the THz band; these are primarily quantum cascade lasers [9], optical parametric oscillators (OPOs) [10], or parametric schemes based on difference frequency generation (DFG) [11]. The latter two can provide high energies and hence, offer the potential to generate high field intensity, tunable THz radiation in a simple and robust design, while operating at room temperature [12]. For single-pass DFG schemes it is beneficial to employ semiconductor materials with high nonlinearity, such as GaP and GaAs [13, 14]. Although these crystals are optically isotropic, the effective interaction length can be substantial by orientation-patterning [15]. Birefringent chalcopyrite ZnGeP₂ (ZGP) and hexagonal GaSe have also been utilized for THz generation [16, 17]. Notably, in ZGP, a peak power of 134 W was reported with relatively broad tunability in the THz region [18]. For high-energy and high average power pumping of these materials it is beneficial to use a mid-infrared source at 2 μm to greatly reduce the one- and two-photon absorption losses and thereby the risk of material damage. Moreover, if the same quantum efficiency as with the near-infrared pumping could be achieved, pumping in the mid-infrared would offer higher power-conversion efficiency for

This article is part of the topical collection “Mid-infrared and THz Laser Sources and Applications” guest edited by Wei Ren, Paolo De Natale and Gerard Wysocki.

✉ R. S. Coetzee
rc@laserphysics.kth.se

- ¹ Department of Applied Physics, Royal Institute of Technology, Roslagstullsbacken 21, 10691 Stockholm, Sweden
- ² School of Physics, Sun Yat-Sen University, Guangzhou 510275, China
- ³ Dipartimento di Ingegneria Industriale e dell'Informazione, Università di Pavia, Via Ferrata 5, 27100 Pavia, Italy

THz generation. For this reason a 2 μm pumped THz source based on GaSe was recently constructed, obtaining average powers of 1.66 μW at 1.48 THz with high repetition rates [17]. A similar pumping scheme, based on a type-II near-degenerate KTP OPO with Poynting walk-off compensation at 2 μm was used to generate THz radiation in orientation-patterned GaAs [19]. However, scaling-up the output energy at 2 μm in this MOPA configuration and employing type-II KTP phase matching would be cumbersome, owing to the relatively low nonlinearity and the Poynting walk-off of the idler.

Two-stage down-conversion schemes pumped with well-established 1 μm lasers, are attractive to reach deeper into the mid-infrared [20, 21]. Down-conversion schemes to the mid-IR often employ quasi-phase-matched KTiOPO_4 (KTP) as the gain material owing to its high-damage threshold, high nonlinearity, good transparency and possibility to fabricate such crystals with large optical apertures [22]. In this work, we report on a highly efficient MOPA configuration with two tunable narrowband outputs at 2 μm by employing periodically poled Rb:KTP (PPRKTP). Energy scaling in this configuration was enabled by the large-aperture PPRKTP crystals [23]. In general, RKTP has a higher laser-induced damage threshold at these wavelength ranges, in the nanosecond range, in comparison to Mg:LN. Mg:LN is favorable for low-to-mid energy applications due to the higher nonlinearity, but suffers in the high-energy multi-millijoule regime. Narrow bandwidth and tunability in our scheme were achieved by application of a chirped volume Bragg grating (VBG) in the OPO stage. The maximum pulse energy generated by the MOPA reached 52 mJ with an average power of 5.2 W with overall efficiency of 36%. The spectral bandwidth of the signal and idler were 36 GHz and the frequency separation between the two pulses could be tuned up to 1.53 THz simply by translating the transversally chirped VBG. Moreover, the OPO stage in the MOPA system was carefully optimized to avoid cascaded four-wave mixing (FWM), which has tendency to emerge in type-0 QPM OPOs operating close to degeneracy [24,

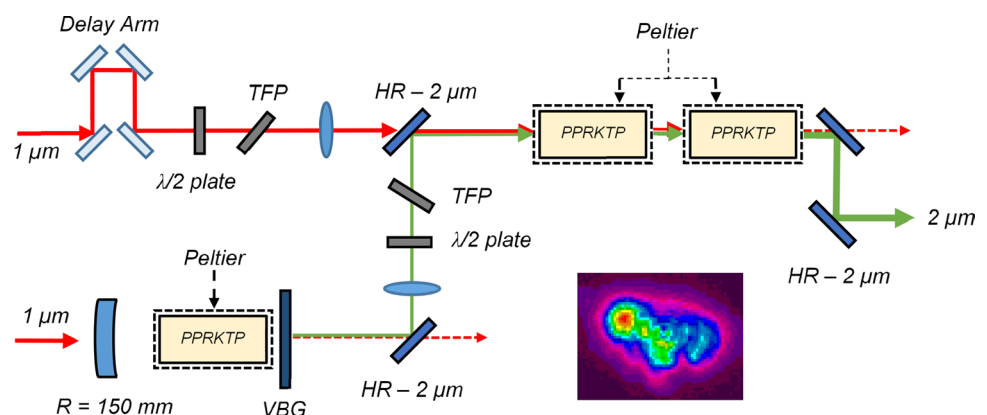
25]. In particular, we show that such FWM processes can be suppressed by limiting noncollinear interactions in the OPO stage.

2 Experimental layout

The MOPA system was pumped by a Q-switched Nd:YAG laser at 1.064 μm (InnoLas Laser GmbH). The laser delivered Gaussian pulses with an available energy of 150 mJ, a repetition rate of 100 Hz and a pulse duration of ~ 10 ns (FWHM). The laser was injection-seeded with a distributed feedback fiber laser to yield single longitudinal mode operation. The power stability of the laser was measured to have an rms value of 0.3%. The beam quality of the pump beam was measured with the 90–10 traveling knife edge method and M^2 values of 3.2 and 3.3 were obtained for the transverse x - and y -axes, respectively. The pump beam profile was measured after beam shaping, and prior to the OPO, and is shown as an inset in Fig. 1. The pump field was linearly polarized along the z -axis of the crystals to utilize the d_{33} nonlinear coefficient of PPRKTP.

The layout of the MOPA system is depicted in Fig. 1. The pump beam is split into two arms, one for the OPO and one for the amplifier stages. The pump beam for the OPO was shaped with spherical and cylindrical optics to correct for astigmatism and produce the desired beam size within the OPO cavity. The OPO gain medium consisted of a single PPRKTP crystal with x - y - z dimensions of $12 \times 7 \times 5$ mm. Rubidium-doped KTP (RKTP) was exploited for fabrication of the periodically poled Rb:KTP samples; thanks to advantageous poling properties [26]. The Rb doping also allows large-aperture PPRKTP crystals to be fabricated, while obtaining good homogeneity of the parametric gain [27]. Large-aperture crystals in turn allow utilizing larger incident beam sizes which are required for high-energy scaling. The crystals were flux grown and periodically poled with a duty cycle of 50%, for first-order QPM. The poling period was 38.85 μm to achieve degenerate type-0 down-conversion

Fig. 1 Experimental layout of the OPO and two-crystal OPA with pump beam profile inset



from 1.064 μm. All crystals used were AR-coated for 1 and 2 μm and temperature-controlled at ~55 °C to operate near degeneracy.

The input coupler of the OPO was a broadband, plane-concave mirror with a radius of curvature of 150 mm and highly reflective over the wavelength range 1.85–2.20 μm. The plane side of the mirror was un-coated, with measured transmission of ~92% at 1 μm. The output coupler was a transversely chirped VBG (Optigrate Inc.). The grating dimensions were x - y - z , $2.2 \times 19 \times 5$ mm, respectively, and the grating had a linear chirp rate along the y -direction of 1.08 nm/mm, corresponding to a tuning range of approximately 21.5 nm around the OPO degeneracy. The VBG was mounted onto a three-axis stage for alignment and OPO tuning. The central wavelength of the VBG was specified to be 2131.3 nm. The diffraction efficiency of the VBG at the central wavelength was specified to be $55 \pm 5\%$ and its damage threshold was specified to ~5 J/cm² at 1 μm for 10 ns long pulses. Both the entry and exit sides of the VBG were AR-coated for 1 and 2 μm radiation and the VBG was temperature-stabilized at 20 °C with a Peltier element.

The cavity design was simulated and arranged to have a signal/idler beam waist radius of 480 μm ($1/e^2$) incident on the VBG. According to calculations, this would yield a reflectivity bandwidth of ~1 nm. The OPO was singly resonant throughout the VBG tuning range, except at the degeneracy point. The total cavity length of the OPO was approximately 55 mm. To optimize the nonlinear conversion, the crystal was placed as close as possible to the VBG, where the size of the pump beam and cavity modes matched.

The OPO output was separated from the depleted pump with a dichroic mirror and reflected towards the amplifier stage. This seed beam was shaped appropriately with spherical CaF₂ lenses to produce a collimated beam and have the seed beam radius of ~2 mm incident on the amplifier. The pump beam of the OPA was collimated and mode-matched to the seed beam. Half-wave plate and thin-film polarizer combinations for 1 and 2 μm allowed separately varying the seed and the pump power in the OPA stage. The number of crystals used in the amplifier was varied and the results were compared. Finally, at the exit of the amplifier, the amplified 2 μm light was separated from the depleted pump field with two dichroic mirrors.

To accurately describe the dynamics of the VBG OPO, a numerical model was developed taking into account the spatial distribution of the pump with its non-symmetric structure. This two-dimensional coupled wave equations had the form:

$$\frac{\partial A_j(x, y, z, t)}{\partial z} = \left[\frac{i}{2k_j} \nabla_{\perp}^2 + \tan \rho_j \frac{\partial}{\partial x} - \alpha_j \right] A_j(x, y, z, t) + \text{NL}_j, \quad (1)$$

where A_j represents the complex amplitude of the pump, signal and idler fields ($j=p, s, i$), k is the wave vector, α is the linear absorption, ρ is the walk-off angle and NL_j are the nonlinear mixing terms which are given by:

$$\text{NL}_p(x, y, z, t) = i \frac{d_{\text{eff}} \omega_p}{c n_p} A_i(x, y, z, t) A_s(x, y, z, t) e^{-i\Delta k z}, \quad (2a)$$

$$\text{NL}_s(x, y, z, t) = i \frac{d_{\text{eff}} \omega_s}{c n_s} A_p(x, y, z, t) A_i^*(x, y, z, t) e^{+i\Delta k z}, \quad (2b)$$

$$\text{NL}_i(x, y, z, t) = i \frac{d_{\text{eff}} \omega_i}{c n_i} A_p(x, y, z, t) A_s^*(x, y, z, t) e^{+i\Delta k z}, \quad (2c)$$

where d_{eff} is the effective nonlinear coefficient, ω_j are the frequencies and n_j are the refractive indices. We assume the forward propagating electric fields take the usual form given by:

$$E_j = \frac{1}{2} \left[A_j e^{-i(\omega_j t - k_j z + \phi)} + A_j^* e^{+i(\omega_j t - k_j z + \phi)} \right]. \quad (3)$$

Since the crystal is periodically poled for QPM, we assume that the wave mismatch vector, given by: $\Delta k = k_p - k_s - k_i$, is equal to zero at degeneracy, as the crystals are poled for these wavelengths. The mismatch vector is recalculated for different signal and idler wavelengths. The above equations consider diffraction, walk-off as well as linear absorption. The equations are accurate for narrowband (single-frequency) fields in the long pulse (nanosecond) regime. Due to these reasons, group velocity terms and dispersion are not included in the model. The input fields are gridded in time as well as space and inserted into Eqs. (1) and (2a, 2b, 2c), which are solved iteratively through the crystal length with the split-step Fourier method and Cash-Karp-Runge-Kutta algorithm. Boundary conditions are applied at the crystal ends to represent the reflection of the cavity mirror and the VBG. The spatial distribution of the pump, measured prior to the OPO, was used as an input to the model with a 128×128 grid. We chose a step size to yield 100 integration points over the length of the crystal. We make use of an averaged beam area for the field mode size, since the beam does not change significantly over the crystal length. To match the simulations with experiments, we altered the value of the nonlinear coefficient d_{eff} to get a best fit (d_{eff} is assumed to be uniform over the whole crystal). Since the interaction is noncritical and collinear, we set the walk-off angle ρ to zero. We omit a full description of the numerical model and refer the reader to references [28–31].

3 Results and discussion

In designing of the MOPA system, we aimed at high overall efficiency without sacrificing spectral or spatial properties of the signal and idler beams while keeping the system as simple as possible. The overall conversion efficiency and simplicity are aided by our choice of not using a high-gain pre-amplifier stage and instead designing the VBG OPO to provide sufficient seed to saturate the OPA. At the same time, the VBG OPO was driven below saturation where the generated output was spectrally narrow and free from unwanted back-conversion processes.

The total output of the VBG OPO, with the largest wavelength difference (signal at 2117 nm and idler at 2141 nm, corresponding to a frequency difference of 1.53 THz), is shown in Fig. 2a.

The threshold of the OPO was found to be around 2.4 mJ of input pump energy. By pumping with a maximum energy of 6.5 mJ, we obtained a total output energy of 1.26 mJ. The pump energies shown in Fig. 2 were corrected for the transmission loss of the pump mirror. At this pump energy, the fluence incident on the VBG was calculated to be 2.5 J/cm². This corresponds to operation of the OPO at around 2.7 times the threshold. An energy stability measurement yielded an rms value of 1.4% for the OPO. The numerical model agrees quite well with the experimentally measured values. In the numerical model,

the linear absorption value was set to 0.5% for all the interacting fields [32] and the output coupling value of the VBG was set to 0.54 for the resonant idler. In this case, the best fit was obtained using a d_{eff} value of 7.6 pm/V. This is less than the ideal value of $d_{\text{eff}} = \frac{2d_{33}}{\pi} \approx 9.8$ pm/V. The numerical model predicts a slightly higher threshold than what was measured, as well as having a marginally larger slope efficiency. The little difference can be attributed to some losses at the resonant wave which were not accounted for in the model.

The maximum conversion efficiency of the OPO was measured to be 20.8%. It is clear from Fig. 2b that the VBG OPO has not reached saturation and back-conversion was hence, insignificant. Similarly, a pump depletion of 21.6% was measured for the OPO at maximum pump energy, which corresponds well with the calculated overall conversion efficiency. The beam profile of the output field was observed with a Pyrocam III camera and compared with the numerical model, as shown in Fig. 3. The profile was recorded at the maximum operating pump energy of 6.5 mJ. As expected, much of the structure of the output beam profile is inherited from the input pump beam profile. This can be seen in the simulated OPO beam at the exit of the OPO. The large-aperture PPRKTP crystals would allow further energy scaling of the OPO output if a higher-energy overall pump budget would be available.

Fig. 2 Measured and simulated output energies of the OPO (a); conversion and pump depletion efficiencies (b)

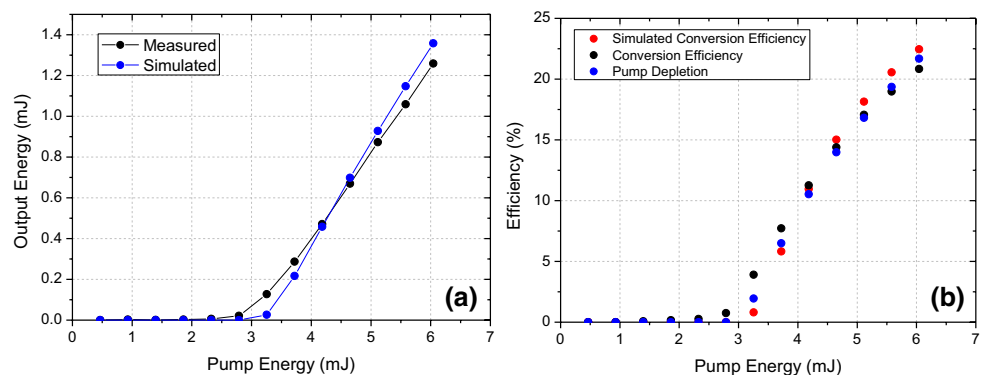
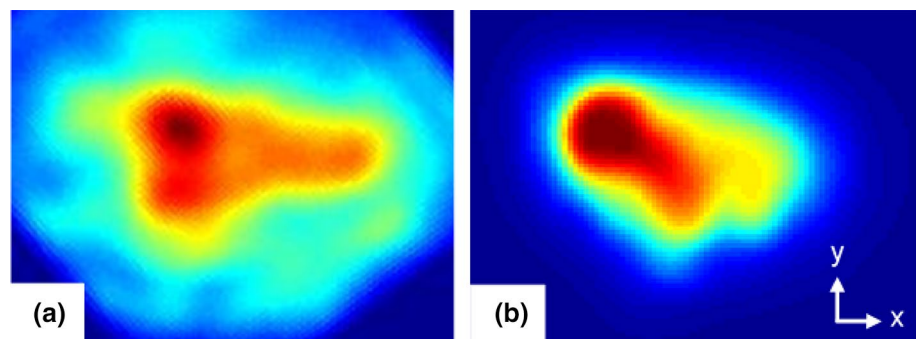


Fig. 3 Far-field measured output beam profile (a); near-field simulated output beam profile of the OPO (b)



The measured far-field of the output OPO beam, seen in Fig. 3a, had M^2 values of 7.7 and 3.4 for the x and y directions, respectively.

The temporal characteristics of the input and depleted pump pulses were measured with an InGaAs photodetector while the 2 μm pulses were measured with a PEM (VIGO) detector. The normalized measured pulse traces are depicted in Fig. 4.

The output trace shown above, is the combined pulse structure of the signal and idler pulses. The FWHM of the output pulse was measured to be around 7.5 ns.

The spectral output of the OPO and the OPA was measured with a Jobin Yvon iHR330 diffraction grating monochromator and a PbSe photodetector. The grating had a groove density of 300/mm and was blazed for wavelengths around 2 μm . The slit size was minimized to 80 μm , allowing a maximum resolution < 0.5 nm in this wavelength band.

The spectrum from the OPO was recorded for varying positions on the VBG. The central wavelengths for the OPO signal and idler as well as the total output energies are shown in Fig. 5a. These measurements were done at a constant OPO pump energy of 6.5 mJ. The measured tuning of the OPO

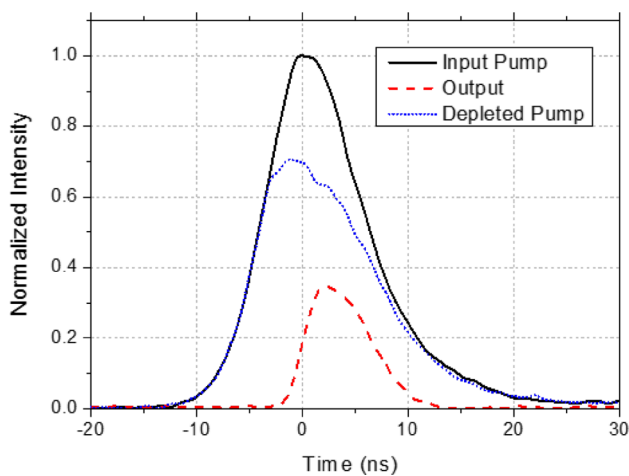
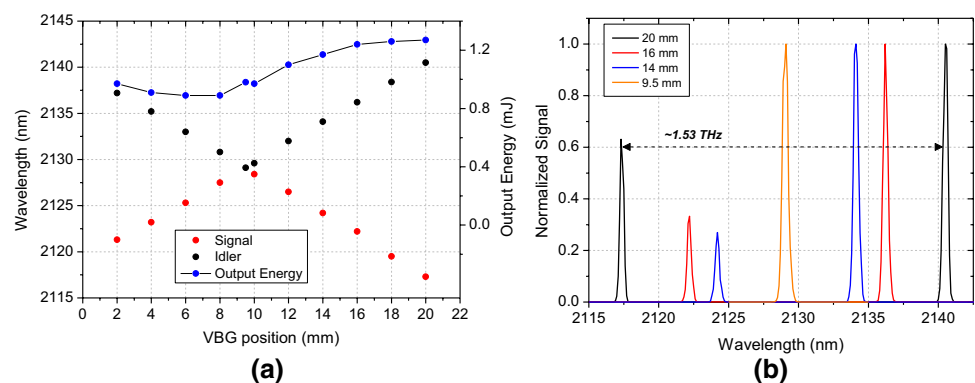


Fig. 4 Measured pulse traces of the OPO

Fig. 5 Signal and idler center wavelengths of the OPO for increasing VBG position (a); measured spectra for different VBG positions, with resonant idler: 9.5 mm (yellow), 14 mm (blue), 16 mm (red), 20 mm (black) (b)

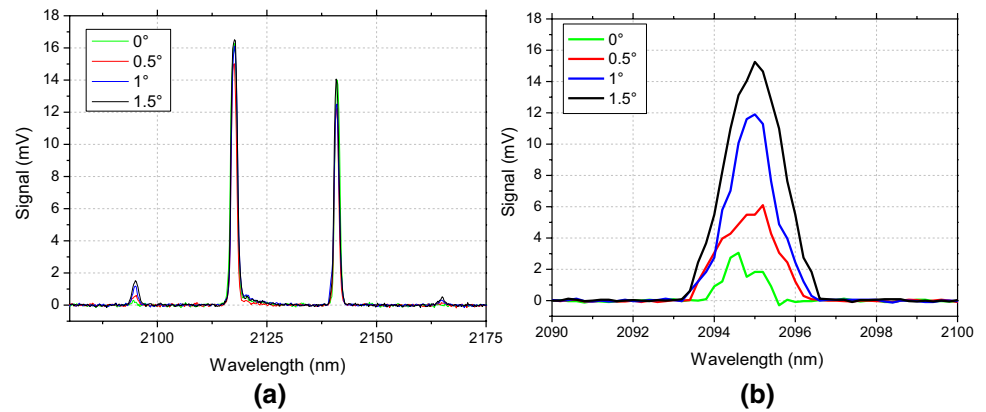


was linear with respect to the VBG position, in agreement with specifications. With this VBG we could choose to oscillate the signal (VBG positions up to “9 mm”) or idler (for larger VBG positions), with the idler-resonant OPO showing somewhat higher output power, presumably owing the specified variation of the VBG reflectivity of $\pm 5\%$. The variation of the OPO output energy for the idler-resonant OPO was 13.4%. A few characteristic measured signal and idler peaks are shown in Fig. 5b. The peaks were symmetric Gaussian and the FWHM bandwidth of each peak was approximately 0.56 nm. No parasitic behavior or four-wave mixing effects were seen in the spectral output of the OPO even when operating at the maximum pump energy of 6.5 mJ [24]. At the far end of the VBG (position 20 mm), the frequency separation between signal and idler was approximately 1.53 THz. At this position of the VBG, it is the idler which is resonant in the cavity.

A broad parametric gain bandwidth experienced by type-0 OPO with VBG spectral narrowing can lead to generation of equi-spaced frequency sidebands owing to cascaded four-wave mixing [25]. The sideband generation process would be enhanced in an OPO with a plane–plane cavity with a large Fresnel number, i.e., with plane mirrors and a large pump beam waist where noncollinear parametric wave components can be readily amplified. To investigate this, we intentionally misaligned the OPO cavity about its vertical axis in incremental steps, and measured the output spectra for each angle, as seen in Fig. 6a, b.

For a well-aligned cavity, the side mode suppression ratio was larger than -29 dB at maximum pump energy. The fact that we did not drive the OPO into saturation also efficiently prevented cascaded processes from taking place. If it should be mentioned, though a careful alignment of the cavity is crucial for the sideband suppression, it is the noncollinear components which will mostly contribute to the sidebands. Indeed, by aligning cavity axis 1° with respect to the pump, we observed decrease in the sideband suppression to about -20 dB. The generated sideband peaks had wavelengths of approximately 2095 and 2165 nm, corresponding to the four-wave mixing processes $2\omega_1 - \omega_s$ and $2\omega_s - \omega_1$, respectively.

Fig. 6 Four-wave mixing peaks in the output spectrum obtained through misalignment of the cavity; (a) first spectral peak magnified by a factor 10 for clarity (b)



Although the four-wave mixing frequency sidebands generated by the MOPA would be detrimental in some spectroscopic applications e.g., in LIDARs, they would not be harmful, but actually, contribute to the THz generation in the DFG process.

The OPO output was steered to propagate collinearly and mode overlap with the pump in the OPA stage. The measured output energy and conversion efficiency of the different OPA stages are given in Fig. 7. At the maximum pump energy of 140 mJ used in the amplifier and with a seed energy of ~ 1.5 mJ, this corresponded to an incident fluence of 2.25 J/cm^2 . It is well below the damage threshold of the crystals, which have been measured to be 10 J/cm^2 at $1 \mu\text{m}$ with nanosecond pulses [33], indicating further power scaling would still be possible. As mentioned, the number of crystals in the amplifier stage was varied, from one to three in total, and the energy output of each configuration was measured. The seed energy from the OPO was 1.5 mJ in each case. For a single-amplifier crystal with a length of 12 mm, and pumping with 140 mJ, we were able to reach a maximum total energy output of 38.3 mJ. This corresponds to an OPA conversion efficiency of 26%. In this case, the OPA did not reach saturation due to insufficiently available pump power. To drive the OPA into saturation and increase the extraction efficiency, a longer OPA crystal would be

required. Therefore, we added a second 12 mm PPRKTP crystal to the OPA stage and re-measured the output. For two crystals (12 + 12 mm), we measured an improvement in the energy yield of OPA, with a maximum output energy of 52 at 140 mJ pump energy, see Fig. 7.

This corresponded to the OPA power-extraction efficiency of 36%. In this case, the amplifier began to saturate at around 60 mJ of the input pump. Extending the OPA length further by adding one more 7 mm-long crystal did not improve the OPA efficiency. This configuration (12 + 12 + 7 mm), actually showed lower performance than the two crystal amplifier. A maximum output energy of 48.5 mJ was reached in this case, with a corresponding conversion efficiency of 33.5%, limited by back-conversion. For this reason, we used the two-crystal amplifier for further measurements. The OPA gain as a function of the seed energy was measured at the pump energy of 60 mJ where the OPA just reached saturation (see Fig. 8a).

The amplifier shows significant saturation for seed energies above 1 mJ. The linear slope of the output energy vs input seed energy for the seed below 0.5 mJ is 12.8, meaning that OPO fluctuations of 1.4% rms would be amplified to 18% rms after the amplifier. At the seed energies above 1 mJ, the slope decreases to 2.6, reducing the output fluctuations to 3.6%. By increasing the pump energy to 140 mJ,

Fig. 7 MOPA output energy vs input pump energy; (a) conversion efficiency of the respective MOPAs (b)

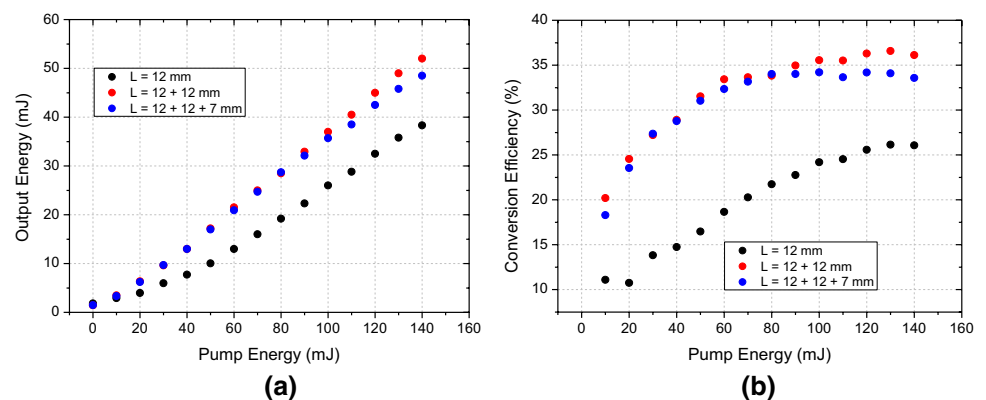
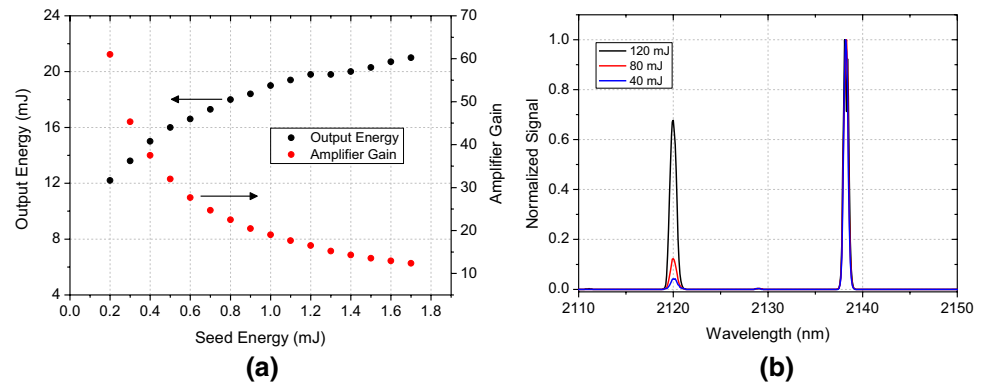


Fig. 8 Amplifier gain and output energy vs seed energy, at constant pump energy of 60 Mj; (a) spectral output of the OPA stage for increasing incident pump energy (b)



the rms fluctuations of the OPA output approach that of the seed OPO. For this reason, we decided to use a seed energy of ~ 1.5 mJ in the amplifier experiments. The output spectra of the amplifier was also measured (Fig. 8b). The spectrum of the OPA stage was measured for increasing pump energies (40, 80 and 120 mJ). As it can be seen in the figure, the amplified signal and idler spectra showed no broadening or wavelength shift even for maximum pump energy and thus, the bandwidth was comparable to that of the OPO output. The OPO is singly resonant on the idler field, and therefore, the majority of the power is initially contained in the idler. This is also the reason why one sees such a great amplification in the signal during amplification, since there is little signal power to begin with, therefore, a greater improvement is easily seen. After significant pumping (post 80 mJ), the amplifier begins to become saturated leading to larger increase shown in Fig. 8b. The saturation is evident from the measured conversion efficiencies in Fig. 7b. At this point, the OPA behavior approaches something more similar to difference frequency mixing (DFM), as opposed to DFG amplification, so more energy flows into the signal field.

4 Conclusions

We have demonstrated a dual-wavelength, tunable, narrowband, high-energy, nanosecond MOPA that is based on large-aperture PPRKTP. We achieved a maximum amplified energy of 52 at 140 mJ of pump energy, corresponding to a mid-IR average power of 5.2 W and an overall conversion efficiency of 36%, even though the pump intensity profile was non-ideal. The spectrum of the amplified output showed no irregularities or indication of degradation. The beam profiles of the amplified fields reflected the structure of the pump beam, but it could be improved utilizing spatial filters. Additionally, the maximum fluence incident on the amplifier (2.25 J/cm^2) is well below the damage thresholds of RKTP, thus further energy scaling should be possible by increasing the pump energy and reducing the crystal length

to avoid back-conversion. Owing to these results, this setup could be an ideal pump for ns DFG THz generation.

Acknowledgements We would like to acknowledge financial support from the Swedish Research Council and the K.A. Wallenberg foundation.

Open Access This article is distributed under the terms of the Creative Commons Attribution 4.0 International License (<http://creativecommons.org/licenses/by/4.0/>), which permits unrestricted use, distribution, and reproduction in any medium, provided you give appropriate credit to the original author(s) and the source, provide a link to the Creative Commons license, and indicate if changes were made.

References

1. V. Petrov, *Opt. Mater.* **34**, 536–554 (2012)
2. J. Peng, *Opt. Eng.* **53**(6), 061613 (2014)
3. A. Godard, *C R Phys.* **8**, 1100–1128 (2007)
4. J. Saikawa, M. Fujii, H. Ishizuki, T. Taira, *Opt. Lett.* Vol. **32**, 2996 (2007)
5. G. Arisholm, Ø Nordseth, G. Rustad, *Opt. Express* **12**(18), 4189–4197 (2004)
6. M. Tonouchi, *Nat. Photonics* **1**, 97–105 (2007)
7. P.U. Jepsen, D.G. Cooke, M. Koch, *Laser Photonics Rev.* **5**, 124–166 (2011)
8. J. Nishizawa, T. Sasaki, K. Suto, T. Yamada, T. Tanabe, T. Tanno, T. Sawai, Y. Miura, *Opt. Commun.* **244**, 469–474 (2005)
9. B.S. Williams, *Nat. Photonics* **1**, 517–525 (2007)
10. J. Kiessling, R. Sowade, I. Breunig, K. Buse, V. Dierolf, *Opt. Express* **17**, 1 (2008)
11. T. Taniuchi, H. Nakanishi, *J. Appl. Phys.* **85**, 12 (2004)
12. Y.J. Ding, W. Shi, *Laser Phys.* **16**(4), 562–570 (2006)
13. W. Shi, Y.J. Ding, *Opt. Lett.* **30**(9), 1030–1032 (2005)
14. S. Ya. Tochitsky, J.E. Ralph, C. Sung, C. Joshi, *J. Appl. Phys.* **98**, 026101 (2005)
15. I. Tomita, H. Suzuki, R. Rungsawang, Y. Ueno, K. Ajito, *Phys. Stat. Sol.* **204**(4), 1221–1226 (2007)
16. J.D. Rowley, D.A. Bas, K.T. Zawilski, P.G. Schunemann, A.D. Bristow, *J. Opt. Soc. Am. B* **30**, 11 (2013)
17. D. Yan, Y. Wang, D. Xu, P. Liu, C. Yan, J. Shi, H. Liu, Y. He, L. Tang, J. Feng, J. Guo, W. Shi, K. Zhong, Y.H. Tsang, J. Yao, *Photonics Res.* **5**, 2 (2017)
18. W. Shi, Y.J. Ding, P.G. Schunemann, *Opt. Commun.* **233**, 183–189 (2004)

19. J. Mei, K. Zhong, M. Wang, P. Liu, D. Xu, Y. Wang, W. Shi, J. Yao, R.A. Norwood, N. Peyghambarian, *IEEE Photonics Technol. Lett.* **28**, 14, (2016)
20. G. Stoeppler, N. Thilmann, V. Pasiskevicius, A. Zukauskas, C. Canalias, M. Eichhorn, *Opt. Express* **20**(4), 4509 (2012)
21. M. Henriksson, M. Tiihonen, V. Pasiskevicius, F. Laurell, *Opt. Lett.* **31**, 1878 (2007)
22. J.D. Bierlein, H. Vanherzeele, *J. Opt. Soc. Am. B*, **6**, 4 (1989)
23. J. Hellström, V. Pasiskevicius, H. Karlsson, F. Laurell, *Opt. Lett.* **25**(3), 174–176 (2000)
24. B. Jacobsson, V. Pasiskevicius, F. Laurell, E. Rotari, V. Smirnov, L. Glebov, *Opt. Lett.* **34**(4), 449–451 (2009)
25. N. Thilmann, B. Jacobsson, C. Canalias, V. Pasiskevicius, F. Laurell, *Appl. Phys. B* **105**, 239–244 (2011)
26. A. Zukauskas, G. Strömqvist, V. Pasiskevicius, F. Laurell, M. Fokine, C. Canalias, *Opt. Mat. Express* **1**, 1319–1325 (2011)
27. A. Zukauskas, N. Thilmann, V. Pasiskevicius, F. Laurell, C. Canalias, *Opt. Mat. Express* **1**(2), 201–206 (2011)
28. A.V. Smith, W.J. Alford, T.D. Raymond, *J. Opt. Soc. Am. B* **12**, 11 (1995)
29. G. Arisholm, *J. Opt. Soc. Am. B* **14**, 10 (1997)
30. A.V. Smith, D.J. Armstrong, M.C. Phillips, *J. Opt. Soc. Am. B* **20**, 11 (2003)
31. T. Debuisschert, *Quant. Semi Class. Opt.* **9**, 209–219 (1997)
32. G. Hansson, H. Karlsson, S. Wang, F. Laurell, *Appl. Opt.* **39**(27), 5058–5069 (2000)
33. R.S. Coetzee, N. Thilmann, A. Zukauskas, C. Canalias, V. Pasiskevicius, *Opt. Mater. Express* **5**(9), 2090–2095 (2015)